

## Article

# High-Throughput Preparation and Characterization of ZrMoTaW Refractory Multi-Principal Element Alloy Film

Qiannan Wang <sup>1</sup>, Hongwang Yang <sup>1</sup> , Xiaojiao Zuo <sup>1</sup>, Yinxiao Wang <sup>1,\*</sup> and Jiahao Yao <sup>2,\*</sup><sup>1</sup> School of Materials Science and Engineering, Shenyang University of Technology, Shenyang 110870, China<sup>2</sup> Beijing Institute of Technology Chongqing Innovation Center, Chongqing 401120, China

\* Correspondence: wangyinxiao@sut.edu.cn (Y.W.); jhyaobitcq@163.com (J.Y.)

**Abstract:** In this work, high-throughput screening technology is applied to four-member refractory multi-principal element alloys (RMPEAs) films with high W content. The exploration of refractory metals such as W is strictly limited by the high melting temperature in this work; a multi-gradient deposition method was introduced to overcome this obstacle. By adjusting the power and distance from the target to the sample, component  $Zr_{11}Mo_{11}Ta_{25}W_{53}$  with the best hardening performance was successfully obtained. The uniformity of the material library was analyzed from the perspectives of phase structure and micromorphology. With the help of Hume-Rothery theory and XRD analysis, it is shown that the film has a stable bcc structure. It is believed that film uniformity, nanoscale size, preferential orientation, surface roughness, and solution mechanism are the pivotal factors to improve hardness performance, especially for high W components. The hardness and modulus of elasticity can reach 20 GPa and 300 GPa, respectively, and the  $H/Er$  and  $H^3/Er^2$  values are 0.067 and 0.065, showing the best wear resistance in many samples.

**Keywords:** refractory multi-principal element alloys; high-throughput screening technology; multi-gradient deposition method



**Citation:** Wang, Q.; Yang, H.; Zuo, X.; Wang, Y.; Yao, J. High-Throughput Preparation and Characterization of ZrMoTaW Refractory Multi-Principal Element Alloy Film. *Materials* **2022**, *15*, 8546. <https://doi.org/10.3390/ma15238546>

Received: 26 October 2022

Accepted: 28 November 2022

Published: 30 November 2022

**Publisher's Note:** MDPI stays neutral with regard to jurisdictional claims in published maps and institutional affiliations.



**Copyright:** © 2022 by the authors. Licensee MDPI, Basel, Switzerland. This article is an open access article distributed under the terms and conditions of the Creative Commons Attribution (CC BY) license (<https://creativecommons.org/licenses/by/4.0/>).

## 1. Introduction

High-entropy alloys (HEAs) were originally proposed by Yeh in terms of chemical composition [1], containing at least five or more elements and mixing them with the same atomic percentages. At present, the study of HEAs is not limited by the original definition, but has expanded it to “complex concentrated alloys (CCAs)” or “multi-principal element alloys (MPEAs)” [2–4].

A high-entropy alloy with more than three refractory metals is called a refractory high-entropy alloy (RHEAs) [2]. RHEAs are considered as the HEAs based on refractory elements, such as Mo, V, Hf, W, Cr, Ta, Nb, Zr, and Ti, and the refractory elements are mostly BCC structures. RHEAs exhibit excellent properties, such as strong corrosion resistance, high strength, good ductility, and good wear resistance, especially high hardness [5–15]. It is reported that the maximum strength of refractory high entropy alloy breaks through the strength limit of traditional refractory alloys. Senkov et al. [10,16] reported both VNbMoTaW and NbMoTaW alloys with a single-phase BCC structure, and the room temperature compressive yield strength ( $\sigma_y$ ) was 1058 MPa and 1246 MPa, respectively. The equal atomic ratio TiZrHfNbTa alloy also has a body-centered cubic (BCC) structure [16], the compressive yield strength  $\sigma_y$  is 929 MPa, and the compressive plastic strain can exceed 50%. Wu et al. [17] reported a novel  $Hf_{25}Nb_{25}Ti_{25}Zr_{25}$  RHEA. The RHEA has a single BCC structure with breaking strength and plastic strain reaches about 969 MPa and 14.9%, respectively.  $TiZr_{0.5}NbCr_{0.5}V$ ,  $TiZr_{0.5}NbCr_{0.5}$ , and  $TiZr_{0.5}NbCr_{0.5}Mo$  alloys with excellent corrosion resistance also have a BCC structure [18].

The traditional “trial and error” method makes minor adjustments to finite element types, which seriously affects the efficiency of research. Regarding the improvement

of efficiency, researchers introduced magnetron sputtering technology in MPEAs and tried to explore a variety of rapid screening methods. Magnetron sputtering, as a typical physical vapor deposition (PVD) technique, can prepare high-quality, completely dense, and well-adhered films. It has been widely used to prepare multi-principal alloys such as AlCrTaTiZr [19], AlCoCrCu<sub>0.5</sub>FeNi [20], BiFeCoNiMn [21], and (TiAlCrNbY)C [22]. Chen et al. [19] first prepared FeCoNiCrCuAl<sub>0.5</sub> and FeCoNiCrCuAlMn nitride films by magnetron sputtering. Zhang et al. [23] used multi-target co-sputtering to obtain gradient materials for Ti-Al- (Fe, Ni, Cr) alloys. Liu et al. [24] used magnetron sputtering to obtain 5700 XRD diffraction patterns from 12 alloy thin film systems. By analyzing an unprecedented amount of experimental data, it was found that a larger full-width at half-maximum ( $\delta q$ ) of the higher glass formation ability (GFA) was related to the first diffraction peak in the XRD diffraction pattern. The alloy film obtained by thin film deposition technology has the advantages of controllable composition and structure, which broadens the way to synthesize RHEAs. Feng et al. [25] deposited TaNbTiW system films with different compositions and explained the structure and mechanical properties of the TaNbTiW films. The maximum hardness and modulus of elasticity obtained from multiple components are 5.2 GPa and 127.2 GPa, respectively. This high-throughput method can effectively reduce the number of bulk alloys prepared, reducing the high consumption of RMPEA in the metallurgical process. As a new refractory alloy system that has not been deeply explored, ZrMoTaW has the potential value of developing high-quality alloys. Moreover, the high melting point metal W content increases the difficulty of exploration. This work will attempt to explore the new alloy and provide a feasible method to facilitate research.

In this work, a novel body-centered cubic Zr-Mo-Ta-W RMPA film was proposed for the first time. The Zr-Mo-Ta-W thin film with gradient component library was prepared by multi-target magnetron co-sputtering. It has high hardness and high wear resistance. The structural stability, surface uniformity, and morphological characteristics of the RMPA were studied. The mechanism of enhancing the mechanical properties of this RMPA is discussed. At the same time, research on the later stage of the film also prospects.

## 2. Experimental Procedure

### 2.1. Multi-Gradient Material Library Preparation

The Zr-Mo-Ta-W quaternary alloy thin films in this work were deposited by a multi-target co-sputtering system (Shenyang Kecheng Vacuum Tech. Co., Ltd., Shenyang, China). Materials can be prepared by sputtering from four elemental targets. The targets are manufactured from hot-pressed elemental powders. The purity of four element targets (Shanghai Institute of Optics and Fine Mechanics, the Chinese Academy of Sciences) exceeded 99.9 percent. The dimensions are 60 mm in diameter and 3 mm in thickness. The center of the target is 100 mm away from the sample surface. The connection between the center of the target material and the center of the sample stage with the plane where the sample stage is located is at an angle of 45°. The film was grown using a commercial single crystal P-Si (100) with a diameter of 50 mm as a substrate, and the schematic diagram of the four-target co-sputtering of the experimental equipment is shown in Figure 1a. The base pressure of the deposition chamber was better than  $9 \times 10^{-4}$  Pa. The target is exposed to air and is prone to oxidation or contamination. To remove the effects of contaminants formed on the target surface, pre-sputtering must be performed at a working pressure of 0.4 Pa for 10 min prior to each deposition process. During the deposition of the film, the sample holder was water-cooled to maintain it at room temperature. The thickness of the film is kept above 1.5  $\mu\text{m}$  by controlling the sputtering time and measuring it by profiler (Alpha-step IQ, KLA, Milpitas, CA, USA).

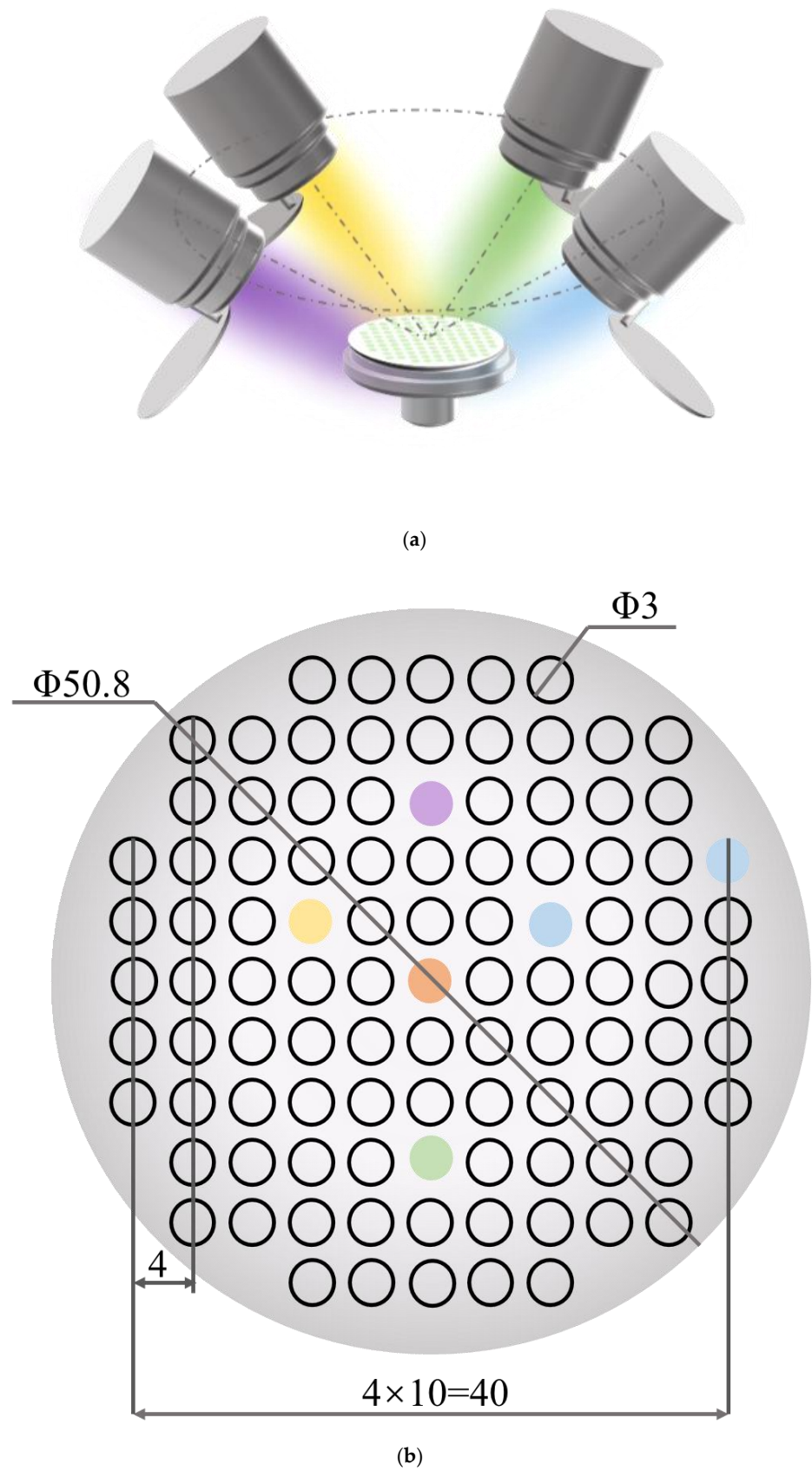


**Figure 1.** (a) Schematic diagram of the four-target co-sputtering. (b) The dimensional design of the aluminum mask plate.

Performance-related high-throughput screening requires the preparation of multi-gradient material libraries by magnetron co-sputtering. A multi-gradient library of materials can be obtained by adjusting the power applied to the targets or by the distance of the target to different locations on the substrate. The tilt of the sputtering guns shown in the figure will cause the distance of the target to different locations on the substrate to be different, so that the incident flux is reduced from near the target to the position away from the target, thus forming a multi-gradient material library. The material library shown in Figure 1a is obtained by separating the alloys by a physical mask covered on the Si substrate. The dimensional design of the mask plate is shown in Figure 1b. There are 101 small round holes on the physical mask, each of which is treated as an independent sampling point of the material library, the so-called “sampling unit”. In other words, 101 independent sample units with completely different compositions can be obtained in one experiment. Table 1 provides the relevant experimental parameters during the preparation of the material library. The screening method provided in this experiment is significantly different from the traditional trial and error method, which may only obtain one alloy per day.

**Table 1.** Experimental parameters of the ZrMoTaW RMPA films.

Samples	Composition (at. %)				Working Gas	Working Pressure (Pa)
	Zr	Mo	Ta	W		
E8	12	23	25	40	Ar	0.4
D11	11	11	25	53		
I5	19	41	20	20		
F6C	21	25	25	29		
C5	18	18	36	28		
E4	29	27	26	18		
Target power (W)	35	30	19	20		

## 2.2. Film Characterization

The composition of the material library (Zr-Mo-Ta-W) was carried out using an energy dispersive X-ray spectrometer (EDS) equipped with field-emission scanning electron microscopy (SEM) (SUPRA 55 SEM, LEO, Oberkochen, Germany). The crystal structure of sample units was analyzed by using a glancing-incidence ( $1^\circ$ ) X-ray diffractometer (X-ray diffraction, XRD, Rigaku D/max-2400, Tokyo, Japan) using the Co  $K\alpha$  radiation at a scanning rate of  $4^\circ/\text{min}$ . The scanning step was  $0.02^\circ$ , and the scanning range was  $30\text{--}90^\circ$ . The hardness and elastic modulus of different sample units were determined by a nano-indentation test (NI, Agilent G200, Agilent Technologies, Santa Clara, CA, USA) which has a Berkovich triangular pyramid indenter. The tip was a circular arc with a radius of 20 nm. The specimen was pressed into with a continuously varying load to obtain a continuous load-displacement curve. To avoid the effect of the substrate on the hardness test of the material, the maximum displacement entering the sample surface was 300 nm, which was  $<10\%$  of the film's thickness.

## 3. Results and Discussion

### 3.1. Composition Gradient Analysis

The composition of obtained film was shown in Figure 2, as Zr, varies from 5 at.% to 55 at.%, Mo varies from 10 at.% to 50 at.%, Ta varies from 10 at.% to 50 at.%, and W varies from 10 at.% to 55 at.%. Figure 3 shows the contour plots of the change of Zr, Mo, Ta, and W content in the film. It was found that as long as the height and the sputtering angle between the target and substrate remained the same, a library of materials shows an unchanged trend of the composition gradient. First, the composition of HEA was predicted

to be close to the intermediate region, and the first sample library region was selected as the film center region F6C. Then, we explored around a central area. In cases where the content of one element is significantly higher than that of the others, a change in the properties of the film can be observed. Even better sample libraries were explored. The specific components of the 6 sample libraries selected are listed in Table 1.

											Ta																						
											A1-	A2-	A3-	A4-	A5-																		
											24,12,	20,12,	15,14,	14,13,	13,12,																		
											43,21	45,23	46,25	44,29	43,32																		
											B1-	B2-	B3-	B4-	B5-	B6-	B7-	B8-	B9-														
											34,11,	29,13,	25,15,	21,16,	17,16,	15,15,	14,14,	13,13,	11,10,														
											35,20	37,21	38,22	39,24	40,27	40,30	38,34	35,39	34,45														
											C1-	C2-	C3-	C4-	C5-	C6-	C7-	C8-	C9-														
											35,16,	30,16,	26,18,	23,18,	18,18,	17,18,	14,17,	13,14,	12,12,														
											32,17	32,22	36,20	35,24	36,28	34,31	33,36	32,41	29,47														
											D1-	D2-	D3-	D4-	D5-	D6-	D7-	D8-	D9-	D10-	D11-												
											40,20,	36,20,	32,21,	27,22,	24,23,	19,22,	17,23,	16,21,	14,17,	12,14,	11,11,												
											28,12	27,17	29,18	31,20	29,24	29,30	28,32	27,36	26,43	25,49	25,53												
											E1-	E2-	E3-	E4-	E5-	E6-	E7-	E8-	E9-	E10-	E11-												
											45,19,	40,20,	34,23,	29,26,	24,24,	19,24,	16,24,	12,23,	12,18,	12,16,	11,14,												
											21,14	22,18	23,20	27,23	27,25	26,31	26,34	25,40	24,46	22,50	20,55												
Zr											F1-	F2-	F3-	F4-	F5-	F6C-	F7-	F8-	F9-	F10-	F11-	W											
											54,18,	48,20,	41,22,	35,24,	27,26,	21,25,	18,25,	15,23,	14,22,	13,21,	10,19,												
											16,12	18,14	20,17	21,20	24,23	25,29	24,33	23,39	21,43	17,49	16,55												
											G1-	G2-	G3-	G4-	G5-	G6-	G7-	G8-	G9-	G10-	G11-												
											53,22,	48,23,	43,25,	36,28,	32,29,	25,30,	20,27,	15,26,	14,25,	12,23,	10,22,												
											15,10	17,12	17,15	18,18	19,20	24,26	24,29	23,36	18,43	17,47	16,52												
											H1-	H2-	H3-	H4-	H5-	H6-	H7-	H8-	H9-	H10-	H11-												
											50,26,	46,26,	41,28,	34,30,	26,32,	20,36,	18,34,	15,33,	13,30,	11,28,	11,26,												
											14,10	15,13	17,14	20,16	22,20	23,21	22,28	20,32	19,38	17,44	15,48												
											I1-	I2-	I3-	I4-	I5-	I6-	I7-	I8-	I9-														
											42,32,	38,33,	30,36,	24,38,	19,41,	17,38,	13,36,	12,35,	10,33,														
											14,12	16,13	16,18	19,19	20,20	20,25	20,31	18,35	14,43														
											J1-	J2-	J3-	J4-	J5-	J6-	J7-	J8-	J9-														
											40,35,	36,37,	29,40,	24,43,	17,46,	16,45,	12,42,	10,39,	9,37,1														
											13,12	14,13	15,16	16,17	17,20	16,23	16,30	17,34	4,40														
											L1-	L2-	L3-	L4-	L5-																		
											27,45,	21,47,	16,50,	15,48,	11,47,																		
											14,14	15,17	16,18	15,22	14,28																		
											Mo																						

Figure 2. The composition of the 101 sample cells in the film.

The corresponding thin film element distribution is shown in Figure 4. Taking sample F6C and sample D11 as an example, the composition of the whole film showed gradient changes, but the local element distribution was uniform. It confirmed local uniformity in the distribution of alloying elements. Khan et al. [26] demonstrated EDS mapping of films grown at different operating pressures and observed uniformity of film deposition. Sha [27] and Malinovskis et al. [28] obtained uniform film by rotating the substrate at a constant speed. In this work, using the four-target co-sputtering technique, it is still possible to obtain the alloy films with the locally uniformly distributed elements. Compared with many researchers such as Sha [27] and Malinovskis et al. [28], the multi-target co-sputtering technology can adjust the chemical composition more easily. Therefore, this technique is a very efficient method for preparing refractory multi-principal alloys (RMPAs).

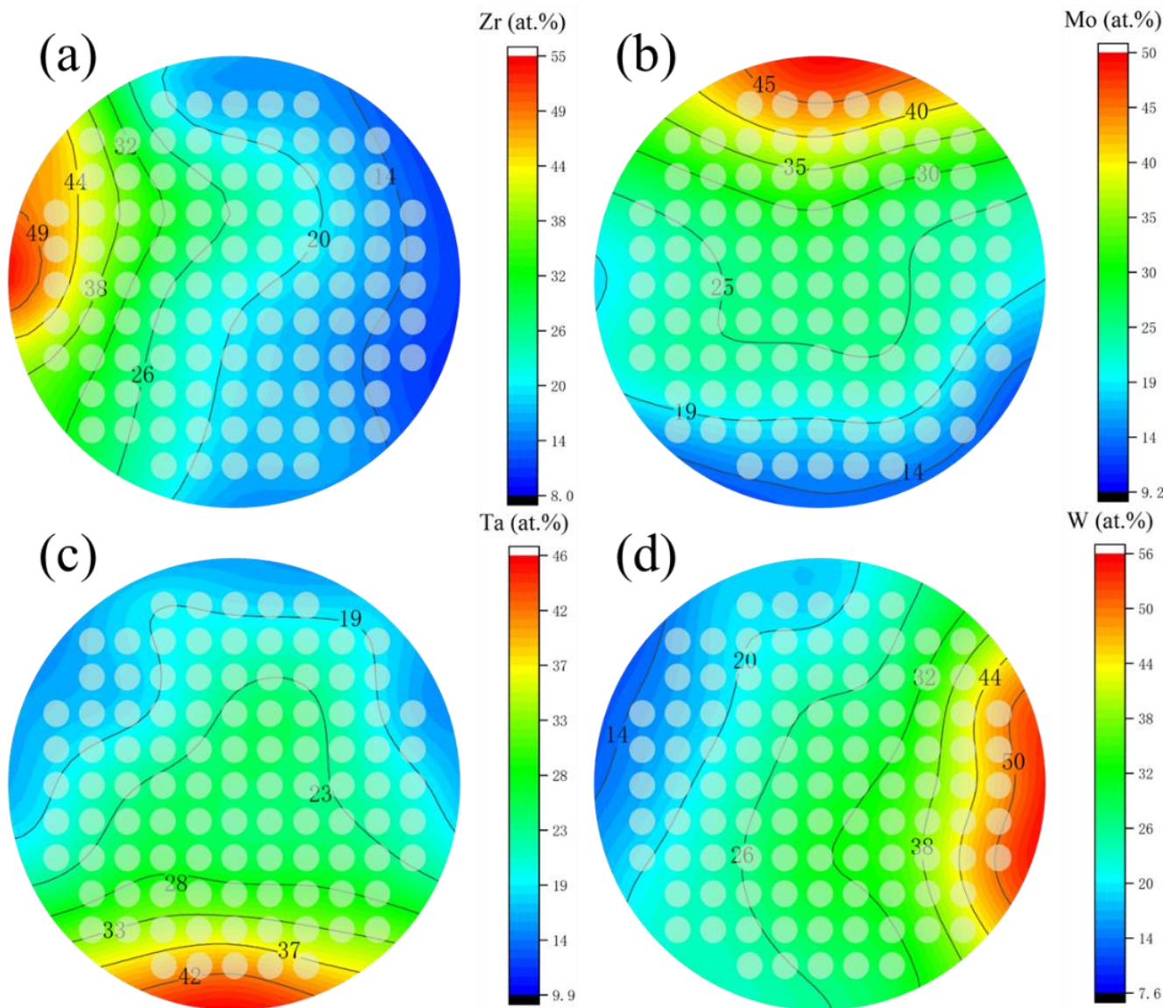


**Figure 3.** Composition gradients of (a) Zr, (b) Mo, (c) Ta, and (d) W of thin film.

### 3.2. XRD Analysis

The XRD pattern of the six samples is shown in Figure 5. According to the XRD patterns, all the samples exhibited BCC single-phase solid solution structure. This can be attributed to the following. 1. All the Zr, Mo, Ta, and W elements have the same BCC structure, and Mo-W, Ta-W, and Mo-Ta are completely mutually soluble [29–31]. W also has a certain solubility in Zr [32]. 2. The high entropy effect caused by multiphase mixing affects the stability of single-phase solid-phase solutions. The increase of entropy can effectively reduce the Gibbs free energy of the whole system and improve stability. This facilitates the intersolubility of elements to form simple single-phase structures instead of multiple phases. In other words, the decrease of Gibbs free energy can obviously reduce the tendency of order and segregation, making the solid solution easier to form and more stable than other ordered phases [33,34]. For the composition design of multi-principal alloys, predicting which elements will be more conducive to the formation of single-phase solid solutions and which elements are more thermodynamically stable when introduced are the first issues to be considered. According to the Hume-Rothery theory, the above issues can be effectively predicted. The empirical criteria are represented by the following:

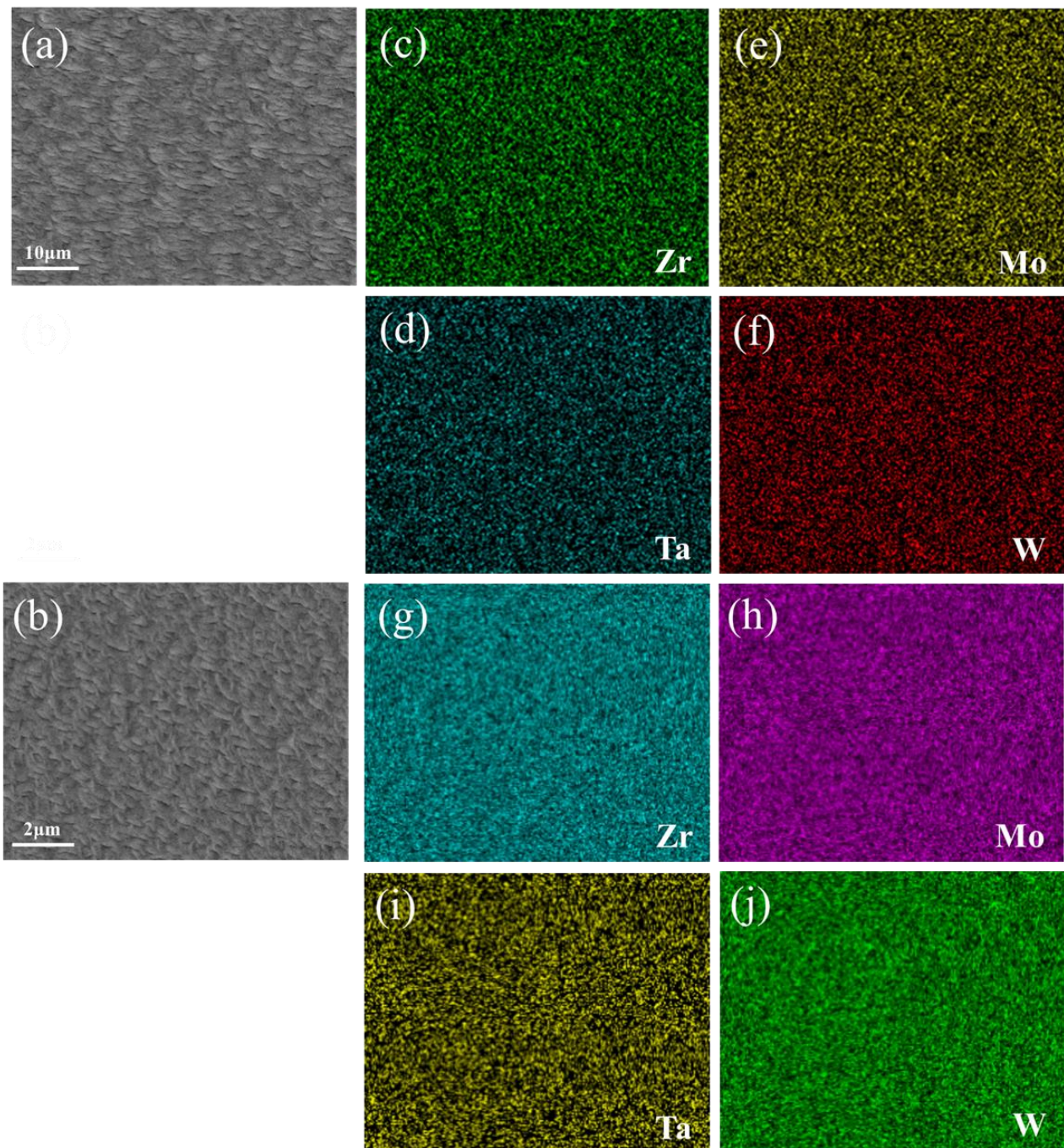


**Figure 4.** (a,b) SEM images of surface morphology of F6C and D11 thin film and (c–j) EDS elemental maps of region shown in (a,b).

The atomic radii and lattice constants of the elements are listed in Table 2. The lattice constant is estimated by  $a = 4r/\sqrt{3}$ . For multi-principal alloys, especially high-entropy alloys, all the principal elements have the same probability to occupy lattice sites to form a solid solution. Therefore, each component element in the alloy system can be regarded as a solute atom, and the serious lattice distortion caused by the large atomic radius difference between so many alloy elements makes the structure of the solid solution in RMPAs distinctive from that of pure metal and traditional alloys.

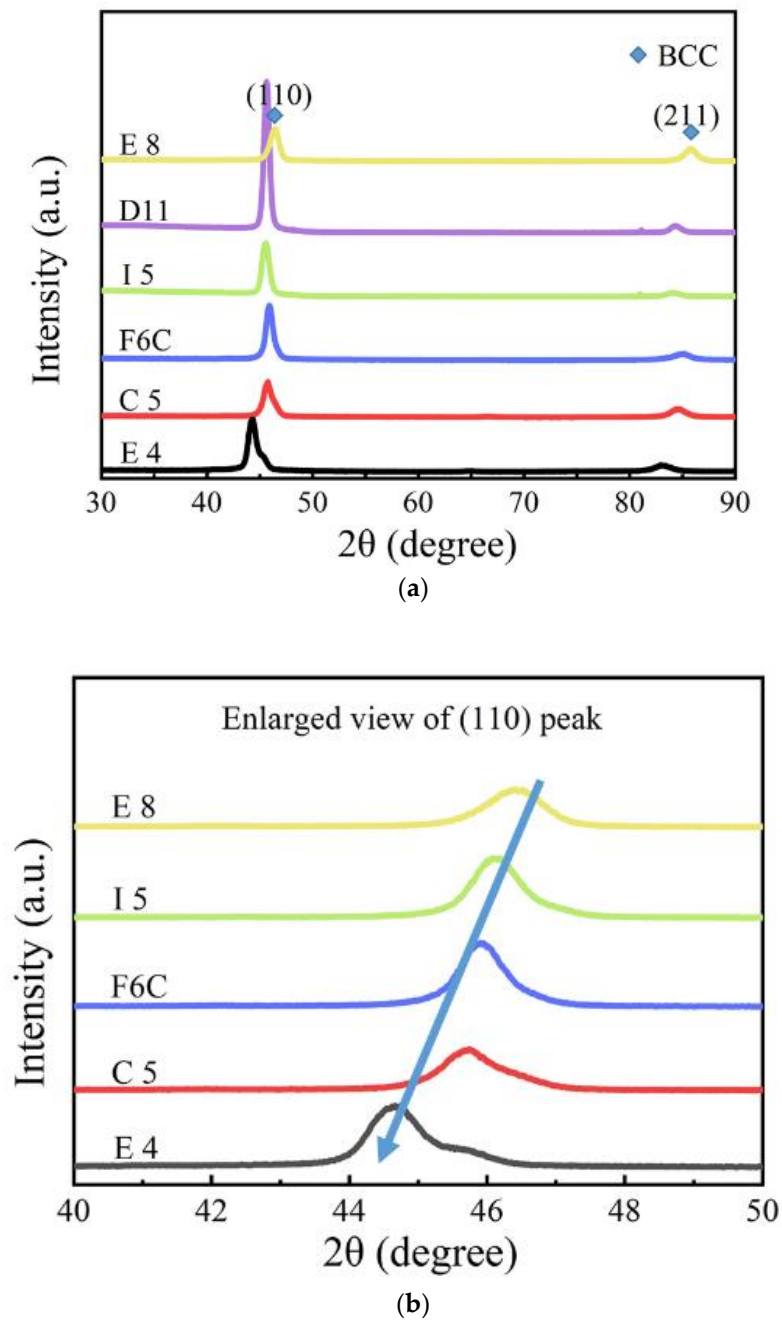


**Figure 5.** (a) XRD patterns of Zr-Mo-Ta-W RMPEA thin films, and (b) enlarged view of samples E8, I5, F6C, C5, and E4 between 40° and 50°.

**Table 2.** Structure, atomic radius, and lattice constant of Zr, Mo, Ta, and W elements in the ZrMoTaW system [10,34–36].

	Element			
	Zr	Mo	Ta	W
Structure	bcc	bcc	bcc	bcc
Radius (nm)	0.160	0.140	0.148	0.141
Lattice constant (nm)	0.3695	0.3233	0.3349	0.3256

As can be seen from the Hume-Rothery rule, the difference between atomic radius  $\delta$  can be expressed as [37,38]:

$$\delta = \sqrt{\sum_{i=1}^n c_i \left(1 - \frac{r_i}{\bar{r}}\right)^2} \quad (1)$$

where  $r_i$  is the atomic radius of the  $i$ th element,  $n$  is the number of elements,  $c_i$  is the atomic percentage of one of the elements in a region of the films,  $\bar{r}$  is the average atomic radius of the film. The average atomic radius ( $\bar{r}$ ) [39] of the film:

$$\bar{r} = \sum_{i=1}^n c_i r_i \quad (2)$$

Thermodynamic parameter  $\Omega$  [40] is further proposed:

$$\Omega = \frac{T_m \Delta S_{mix}}{|\Delta H_{mix}|} \quad (3)$$

$$T_m = \sum_{i=1}^n c_i (T_m)_i \quad (4)$$

where  $T_m$  is the theoretical melting point of an alloy,  $(T_m)_i$  is the melting point of the  $i$ th component of alloy,

It has been reported that the conditions for the formation of a single solid solution phase are  $\Omega \geq 1.1$  and  $\delta \leq 6.6\%$  [40]. Zhang et al. [37,38] also proposed that the mixing enthalpy  $\delta H_{mix}$  of the alloy in the liquid state can also be used as a criterion for solid solution formation:

$$\Delta H_{mix} = \sum_{i=1, i \neq j}^N 4\delta H_{ij}^{mix} X_i Y_j \quad (5)$$

In the equation,  $\delta H_{ij}^{mix}$  is the mixing enthalpy of the  $i$ th and  $j$ th components. When  $-15 \leq \delta H_{mix} \leq +5$  KJ/mol and  $\delta \leq 5\%$ , it is beneficial to form a disordered solid solution.

Valence electron concentration (VEC) to evaluate the stability of the solid solution phase was proposed by Guo et al. [35].

$$VEC = \sum_{i=1}^n c_i (VEC)_i \quad (6)$$

where  $VEC_i$  is the valence electron concentration of the  $i$ th component. When  $VEC \geq 8.0$ , a single-phase FCC structural phase is formed; when the  $VEC \leq 6.87$ , a single-phase BCC structural phase is formed; when  $6.87 \leq VEC \leq 8.0$ , a duplex solid-solution phase of FCC and BCC structures is formed.

The parameters such as thermodynamic parameters ( $\Omega$ ), atomic size mismatch ( $\delta$ ), and valence electron concentration (VEC) of Zr-Mo-Ta-W RMPAs are listed in Table 3. For the Zr-Mo-Ta-W alloy system, thermodynamic parameters  $\Omega \geq 1.1$ ,  $\delta \leq 6.6\%$ , and  $VEC \leq 6.87$ , which satisfied the BCC solid-solution phase formation conditions. The mixed entropy ( $\delta S_{mix}$ ) obtained in the table is also significantly higher than that of conventional alloys. This means that the Zr-Mo-Ta-W RMPA films prepared in this experiment also have high mixed entropy, which helps to form a simple disordered solid-solution phase in the alloy system.

As the XRD diffraction pattern is shown, the (110) peak of the F10 film is higher, which indicates that the film exhibits an optimal orientation of (110). Some theories suggest that the grain surface grows slowly when the merit orientation is preferred. The relative degree of optimal orientation of the deposited coating can be expressed by the texture coefficient (TC), which is calculated as follows [41]:

$$TC = \frac{I_{(hkl)} / I_{0(hkl)}}{(1/n) / \sum I_{(hkl)} / I_{0(hkl)}} \quad (7)$$

where  $I_{(hkl)}$  is the peak strength of the film in the XRD diffraction pattern;  $I_{0(hkl)}$  is the standard strength in the JCPDF database;  $n$  is the total number of diffractive surfaces. When the TC of the diffractive plane is unity, the crystal orientation distribution is random. When the TC of the  $(hkl)$  surface is greater than unity, it indicates that there is a merit-based orientation. The larger the value of TC, the greater the degree of merit orientation. The calculated TC values are listed in Table 4. From the TC value, E8 presents a (211) merit orientation, and most of the other units of the film present a (110) preference orientation, and in E8, the (110) degree of preference orientation is the greatest.

**Table 3.** Thermodynamic parameters of the ZrMoTaW RMPEA thin films with different compositions.

Samples	Composition	Atomic Size Difference (%)	Mixing Enthalpy (kJ·mol <sup>-1</sup> )	Mixing Entropy (kJ·mol <sup>-1</sup> )	Theoretical Melting Point (K)	Thermodynamic Parameter (Ω)	Valence Electron Effect (VEC)
		δ (%)	δH (kJ·mol <sup>-1</sup> )	δS (kJ·mol <sup>-1</sup> )	Tm (K)	Ω	VEC
E8	Zr <sub>12</sub> Mo <sub>23</sub> Ta <sub>25</sub> W <sub>40</sub>	4.11	−5.98	10.85	2657	4.82	5.51
D11	Zr <sub>11</sub> Mo <sub>11</sub> Ta <sub>25</sub> W <sub>53</sub>	5.49	−6.32	9.72	2764	4.25	5.53
I5	Zr <sub>19</sub> Mo <sub>41</sub> Ta <sub>20</sub> W <sub>20</sub>	5.21	−5.54	11.01	2429	4.83	5.42
F6C	Zr <sub>21</sub> Mo <sub>25</sub> Ta <sub>25</sub> W <sub>29</sub>	4.32	−6.10	11.47	2503	4.71	5.33
C5	Zr <sub>18</sub> Mo <sub>18</sub> Ta <sub>36</sub> W <sub>28</sub>	3.90	−5.93	11.15	2564	4.82	5.28
E4	Zr <sub>29</sub> Mo <sub>27</sub> Ta <sub>26</sub> W <sub>18</sub>	4.45	−5.57	11.40	2531	5.18	5.83

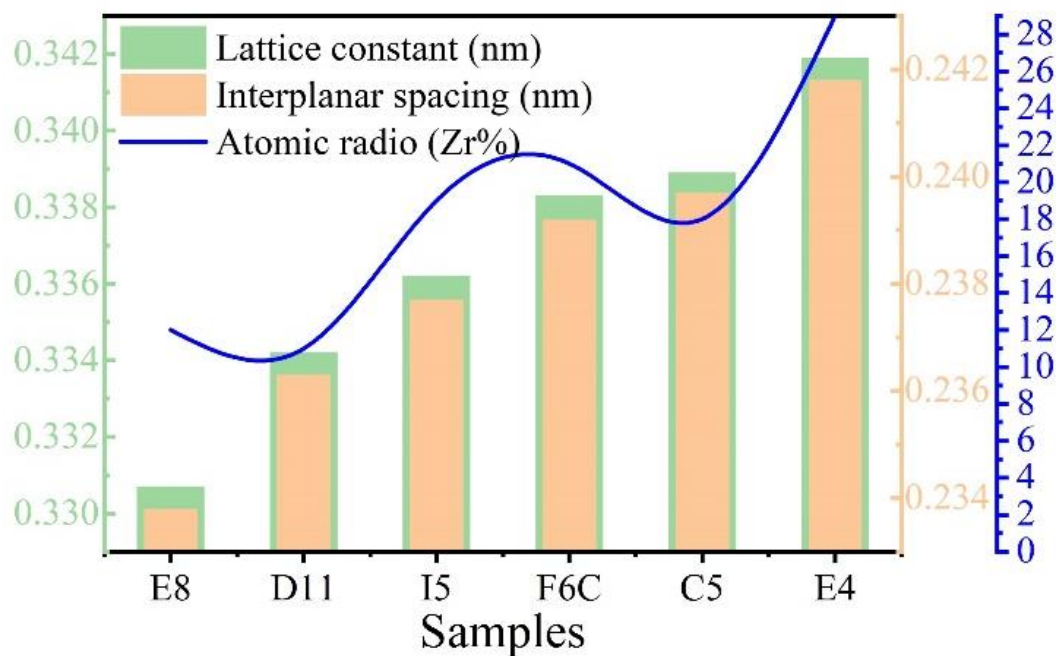
**Table 4.** Texture coefficient of (110) and (211) planes.

	E8	D11	I5	F6C	C5	E4
(110)	0.91	1.77	1.56	1.52	1.15	1.48
(211)	1.08	0.23	0.44	0.48	0.85	0.51

As shown in Figure 5b, (110) diffraction peaks shifted to a lower angle with increasing Zr from sample E8 to sample E4. When the XRD diffraction angle decreases, the surface spacing increases, which indicates that the lattice constant of the ZrMoTaW alloy increases [42]. The average atomic radius of each component is calculated using Equation (4) and the lattice constant of the different thin films is estimated by the equation  $a = 4\bar{r}/\sqrt{3}$ . Then, according to the relation of the Bragg Law  $2d\sin\theta = n\lambda$  ( $\lambda = 0.179021$  nm) and the interplanar spacing  $d_{hkl} = a/\sqrt{h^2 + k^2 + l^2}$ , the diffraction angles  $\theta$  can be calculated. The calculated average atomic radius, lattice constant, interplanar spacing  $d_{hkl}$ , diffraction angle  $\theta$  (110), and  $d$  values of the samples E8, D11, I5, F6C, C5, and E4 are listed in Table 5. In the table, the average atomic radius is relatively small at  $0.146 \pm 0.003$  nm, and the crystal plane spacing is maintained at  $0.237 \pm 0.005$  nm. The Zr content increases and the corresponding mean atomic radius increases from 0.1432 nm to 0.1481 nm. Figure 6 shows the lattice constant and crystal plane spacing of the selected compositions. The content of Zr elements showed an upward trend, and its lattice constant and crystal plane spacing also showed a corresponding trend. Therefore, it is considered that in Figure 5b, the main reason for the small angular shift of the diffraction peak in the alloy ZrMoTaW is that the alloying elements with large atomic radii enter the lattice structure, causing lattice expansion and increasing in  $d$  value.

**Table 5.** Average atomic radius, lattice constant, interplanar spacing, and diffraction angle (110).

Samples	Composition	Average Atomic Radius (nm)	Lattice Constant (nm)	Interplanar Spacing (nm)	Diffraction Angle ( $\theta$ )
		$\bar{r}$ (nm)	$a_n$ (nm)	$d_{hkl}$ (nm)	( $\theta$ )
E8	Zr <sub>12</sub> Mo <sub>23</sub> Ta <sub>25</sub> W <sub>40</sub>	0.1432	0.3307	0.2338	22.51
D11	Zr <sub>11</sub> Mo <sub>11</sub> Ta <sub>25</sub> W <sub>53</sub>	0.1447	0.3342	0.2363	22.26
I5	Zr <sub>19</sub> Mo <sub>41</sub> Ta <sub>20</sub> W <sub>20</sub>	0.1456	0.3362	0.2377	22.12
F6C	Zr <sub>21</sub> Mo <sub>25</sub> Ta <sub>25</sub> W <sub>29</sub>	0.1465	0.3383	0.2392	21.97
C5	Zr <sub>18</sub> Mo <sub>18</sub> Ta <sub>36</sub> W <sub>28</sub>	0.1468	0.3389	0.2397	21.73
E4	Zr <sub>29</sub> Mo <sub>27</sub> Ta <sub>26</sub> W <sub>18</sub>	0.1481	0.3419	0.2418	21.73

**Figure 6.** The lattice constant, interplanar spacing, and atomic radius (Zr%) of Zr-Mo-Ta-W RMPEA thin films.

### 3.3. Surface and Cross-Sectional Morphology

The surface and cross-sectional morphologies of the ZrMoTaW quaternary thin film are shown in Figure 7. The Zr-Mo-Ta-W RMPA film with different compositions all exhibited a flake-like surface morphology. All the cross-section morphologies are typical dense columnar structures, as shown in Figure 7a–d. The grain sizes of the different components obtained in Table 6 according to the Scherrer equation:

$$D = \frac{k\lambda}{\beta \cos\theta} \quad (8)$$

where  $k$  is the shape factor ( $k = 0.943$  [43]),  $\beta$  is the full width at half-maximum. The grain size of the ZrMoTaW film is between 10 nm and 15 nm. Yeh et al. [1] suggested that diffusion for phase separation in HEAs is sluggish. The difficulty of displacement diffusion is affected by the elements in these alloys and the interaction between the formation and growth rates of atomic nuclei, which lead to the formation of ultrafine grains. On the other hand, high deposition rates also refine grains [44].

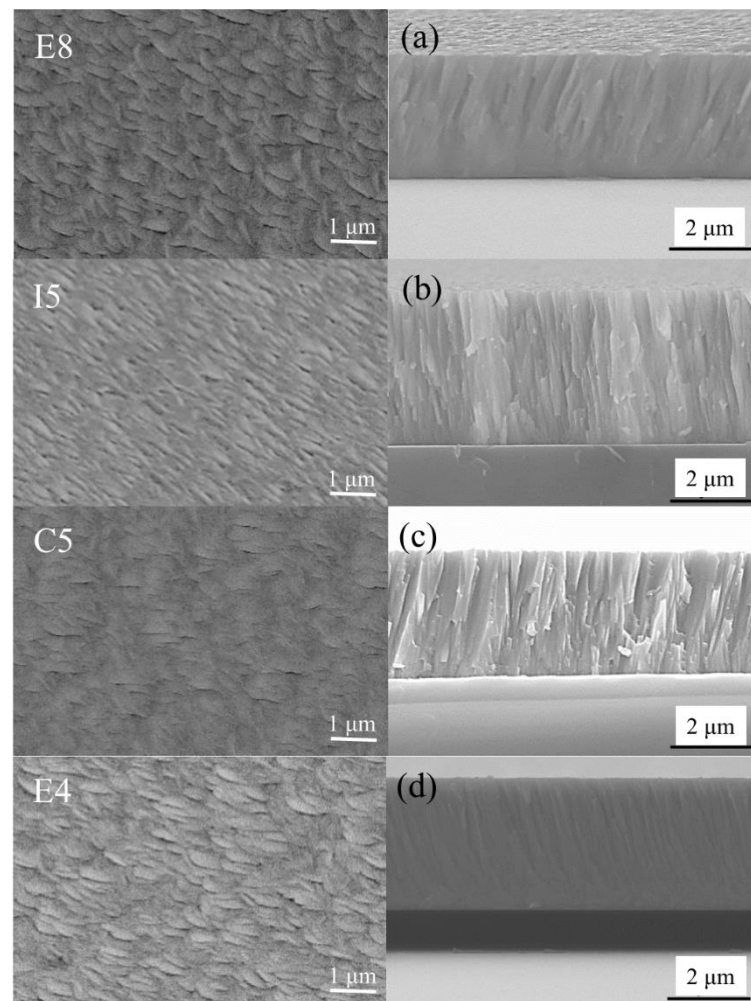


**Figure 7.** SEM plan-view morphology and cross-sectional of ZrMoTaW RMPEA thin films: E8, (a)  $Zr_{12}Mo_{23}Ta_{25}W_{40}$ ; I5, (b)  $Zr_{19}Mo_{41}Ta_{20}W_{20}$ ; C5, (c)  $Zr_{18}Mo_{18}Ta_{36}W_{28}$ ; E4, (d)  $Zr_{29}Mo_{27}Ta_{26}W_{18}$ .

**Table 6.** Mean grain size, thickness, and deposition rate of ZrMoTaW RMPEA thin films.

Samples	Composition	Grain Size (nm)	Thickness ( $\mu\text{m}$ )	Deposition Rate (nm/min)
E8	$Zr_{12}Mo_{23}Ta_{25}W_{40}$	11.94	3.005	8.35
I5	$Zr_{19}Mo_{41}Ta_{20}W_{20}$	11.01	3.392	9.42
C5	$Zr_{18}Mo_{18}Ta_{36}W_{28}$	10.90	2.909	8.08
E4	$Zr_{29}Mo_{27}Ta_{26}W_{18}$	10.82	3.252	9.03

In Figure 2, sample I5 and sample E4 are close to the Mo target and Zr target, and sample E8 and sample C5 are close to the W target and Ta target. The deposition rate can be expressed in terms of deposition thickness per unit of time. Combined with the experimental parameters in Table 1 and the calculation of the deposition rate in Table 6, It can be seen that the deposition rate and target power of sample I5 and sample E4 are higher than those of sample E8 and sample C5. In Table 6, the deposition rate is reduced from I5 9.42 nm/min, E4 9.03 nm/min to E8 8.35 nm/min, and C5 8.08 nm/min. The increase in sputtering power will relatively increase the deposition rate of the film and thus promote grain refinement. In summary, the formation of nanocrystals is promoted by the combination of various factors such as slow diffusion effect, deposition rate, sputtering power, etc.

### 3.4. Surface Roughness

The AFM surface topography of samples E8, I5, C5, and E4 is shown in Figure 8. Figure 8 shows a distinct flake structure on the surface of the alloy film. This is consistent with the topography results presented in Figure 7. The scanning height is 0–130 nm, and the scanning range is in the area of  $5 \times 5 \mu\text{m}$ . Due to the different atomic radii of the elements, there is a certain variation range of roughness Ra, about 11–16 nm, and the film is relatively smooth overall. The sample with the lowest Zr atom ratio, E8, had the lowest roughness of 11.88 nm, while sample E4 had the highest surface roughness of 15.94 nm due to the mixing of more Zr elements with large atomic radii. Therefore, we believe that the surface roughness of RMPAs is mainly affected by the atomic radius of the element, and as the content of elements with large atomic radii increases, the roughness would be higher. The following two factors also affect the surface roughness of the film. First, the mask plate used in this work caused a blocking effect on the sputtering particles, thereby affecting the deposition uniformity of the sample library. Second, the surface roughness is affected by the deposition rate of the sample [45]. The roughness of E8 is significantly lower than that of E4, and the deposition rate of E8 in Table 6 is 8.35 nm/min, which is significantly lower than that of E4 at 9.03 nm/min.

### 3.5. Mechanical Properties

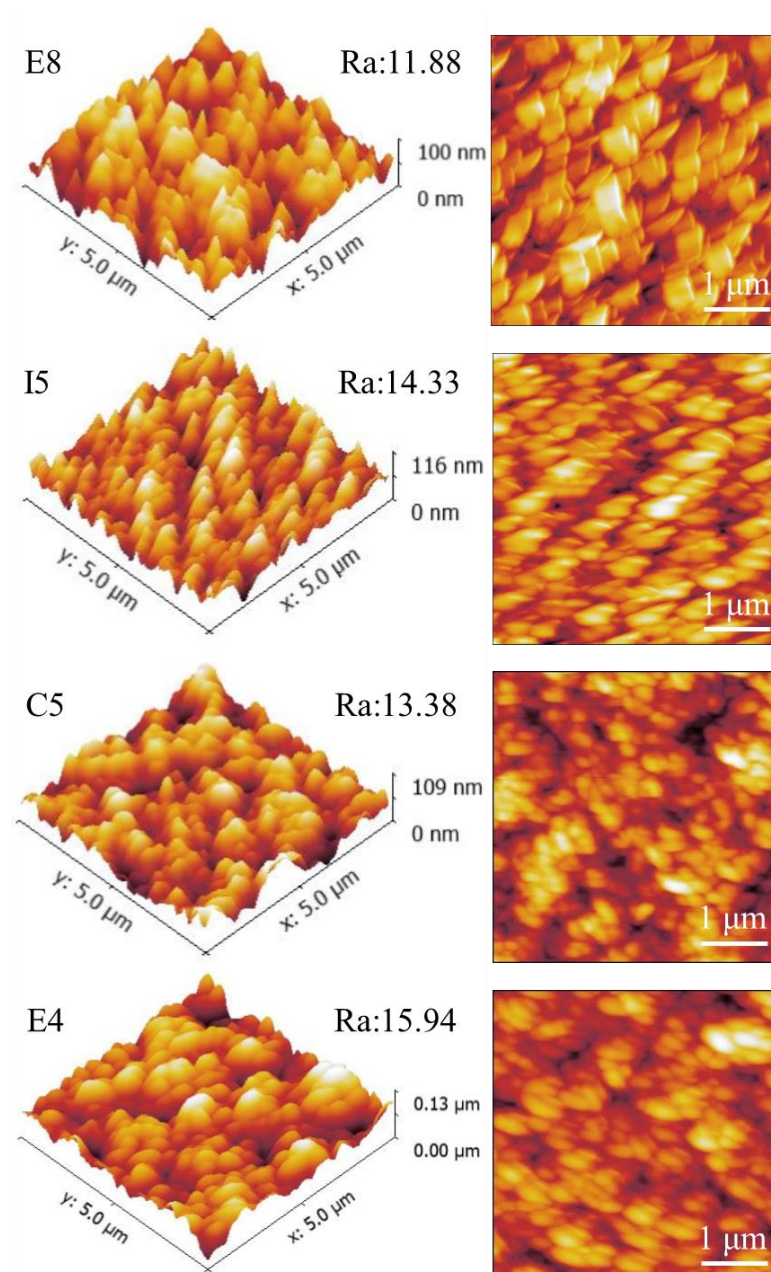
The load–displacement curves of the ZrMoTaW film on the Si substrate are shown in Figure 9. In the two illustrations in Figure 9, it can be observed that there is a slight “pop-in” phenomenon near 125 nm and 180 nm, but the load changes evenly with the overall displacement. The load–displacement curves of the TaNbHfZr thin films obtained by nanometer indentation by Song et al. showed an obvious “pop-in” phenomenon at the displacements of 40 nm and 65 nm, respectively, and it was caused by uneven deformation triggered by partial crystallization [46].

Figure 10 summarizes the hardness and elastic modulus of the ZrMoTaW RMPEA gradient film. For D11  $\text{Zr}_{11}\text{Mo}_{11}\text{Ta}_{25}\text{W}_{53}$ , the hardness can reach 20 Gpa, and the elastic modulus exceeds 300 Gpa. Compared with the refractory metals reported in Table 7 [10,36,46–52], the ZrMoTaW RMPEA thin film can reach much higher hardness than other materials. We attribute the excellent mechanical properties mainly to: (1) The composition distribution of ZrMoTaW RMPEA film is locally homogeneous. The four-target co-sputtering forms a locally evenly distributed chemical composition, as shown in Figure 4, which reduces the defect of the film and improves the mechanical properties of the film. (2) ZrMoTaW RMPEA films inherit the excellent properties of high strength and hardness of nanocrystals [53,54]. The structure of the thin film is nanocrystalline, and the grain size does not exceed 15 nm. (3) The (110) preferential orientation is conducive to improving the hardness of ZrMoTaW RMPEA film [55,56]. It can be seen from the XRD pattern that the sample  $\text{Zr}_{11}\text{Mo}_{11}\text{Ta}_{25}\text{W}_{53}$  has a much higher peak strength than other components, and its hardness is also much higher than that of other components. (4) The surface roughness affects the hardness of the film. As Jiang et al. discovered in their exploration of the effect of film surface roughness on the nanoindentation experiments, the nano hardness of rough films is generally lower than the predicted value of smooth films [57]. The peak strengths of E8 and E4 in this work are almost identical, but the roughness of E4 is significantly greater than that of E8. In Figure 10, E4 has the lowest hardness, and the hardness of E8 is significantly greater than that of E4. This is consistent with the reported experimental results of Jiang et al. The large surface roughness of the film means that the size of the micro-holes between the particles increases, which affects the density of the film and leads to a decrease in hardness [42,57–59]. (5) Solid solution strengthening significantly affects the hardness of multi-component alloy films. Lattice mismatch can seriously affect the mechanical properties of the alloy, in addition to being related to the phase stability described in Section 3.1 [2,60,61]. Due to the variety of elements, HEAs inevitably produce lattice distortion. A large number of dislocations are generated during deformation, and the interaction of these dislocations with the local

stress field of the solute atoms causes the MPEAs to produce solid solution strengthening. The interaction forces can be inferred by Equation (9):

$$F = Gb^2\delta = Gb^2[\beta\delta_a + \delta_G] \quad (9)$$

where  $G$  represents the shear modulus of the alloy,  $b$  is the magnitude of the Burgers Vector,  $\beta$  is a constant, the size mismatch  $\delta_a = \frac{1}{a} \frac{da}{dc}$ , the modulus mismatch  $\delta_G = \frac{1}{G} \frac{dG}{dc}$ , and  $G$  is the shear modulus of the alloy. The constant  $\beta$  is related to the spiral dislocation and blade dislocation and local stress field caused by solute atoms [62,63]. It has been reported that  $\beta$  is 2–4 for spiral dislocations and  $\beta \geq 16$  for blade dislocations [62]. Since the alloy studied in this paper shows BCC structure, the spiral dislocation and the blade dislocation may exist at the same time, so the value of  $\beta$  is 9 [16].



**Figure 8.** AFM surface roughness of ZrMoTaW RMPEA thin films: E8  $Zr_{12}Mo_{23}Ta_{25}W_{40}$ ; I5  $Zr_{19}Mo_{41}Ta_{20}W_{20}$ ; C5  $Zr_{18}Mo_{18}Ta_{36}W_{28}$ ; E4  $Zr_{29}Mo_{27}Ta_{26}W_{18}$ .

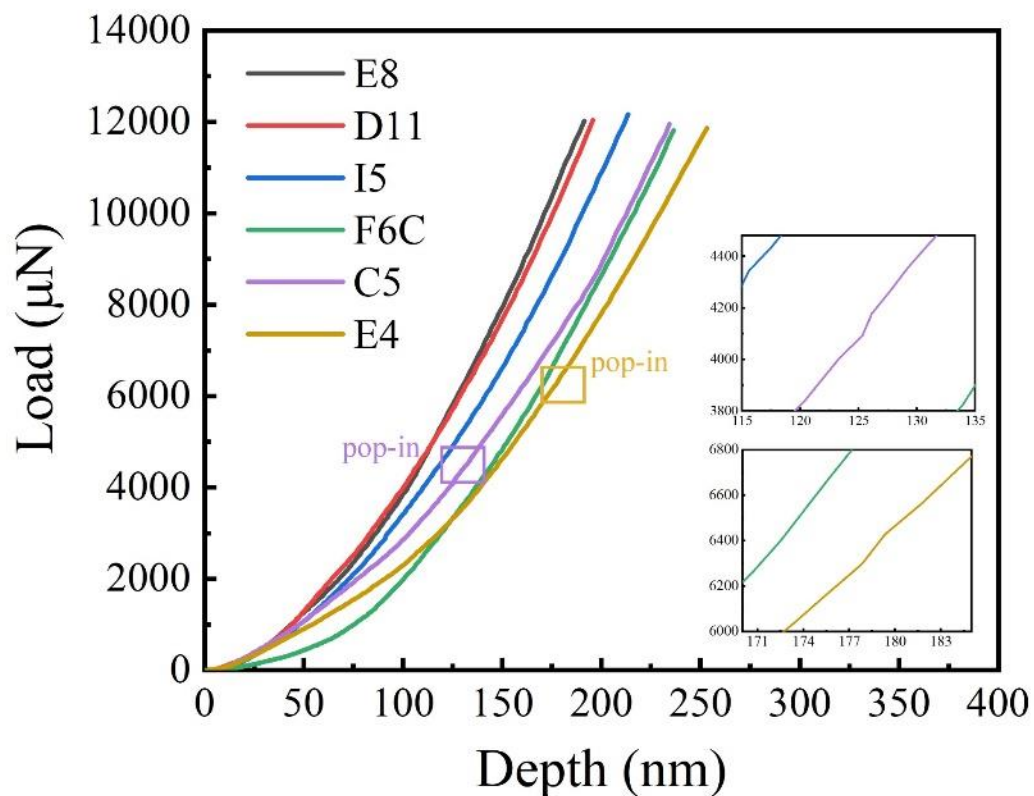


Figure 9. Typical load–displacement curves of ZrMoTaW film and the enlarged inset shows the “pop-in” phenomenon for  $Zr_{18}Mo_{18}Ta_{36}W_{28}$  and  $Zr_{29}Mo_{27}Ta_{26}W_{18}$ .

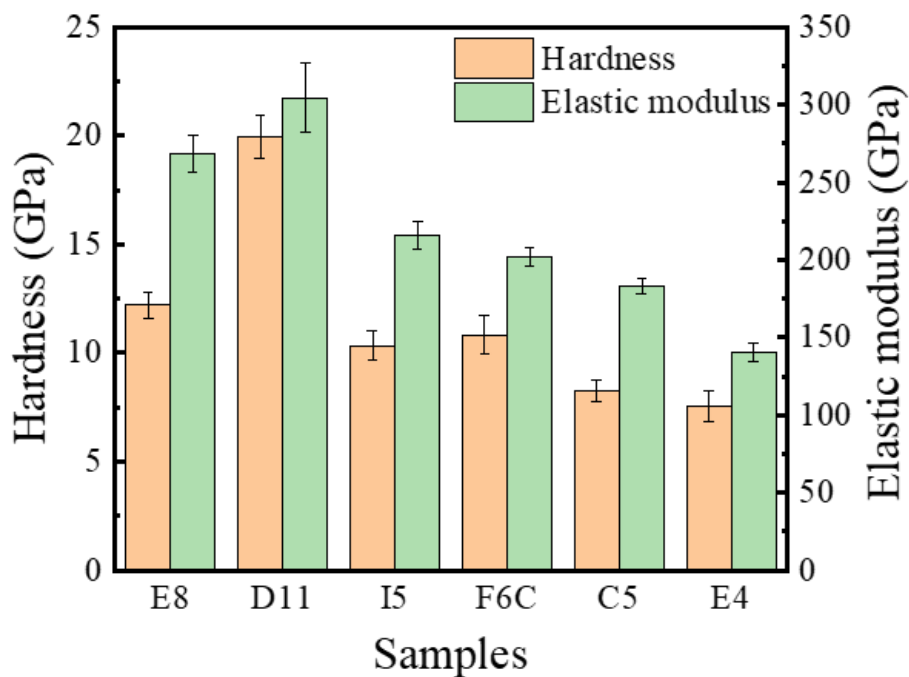


Figure 10. Nano hardness and elastic modulus ZrMoTaW RMPEA thin films: E8, D11, I5, F6C, C5, E4.

**Table 7.** The hardness values of refractory metals, RMPEAs blocks, and RMPEAs thin films.

Metals	Hardness (GPa)	Reference
Bulk	Zr	9 [47]
	Mo	6 [48,49]
	Ta	2 [48,50]
	W	8 [49,50]
	TaNbHfZr	3.58 [36]
	NbMoTaW	4.46 [10]
	NbMoTaWV	5.25 [10]
Films	NbMoTaW	13.5 [63]
	TaNbHfZr	15.3 [46]
	TiVCrAlZr	8.2 [52]
	This work	20

The contribution of lattice distortion to solid solution strengthening can be assessed by quantitative calculations. In multi-principal alloys of single-phase solid solutions, lattice distortion and modulus distortion are the main causes of solid solution strengthening, which can be expressed in  $\delta\sigma_s$  :

$$\delta\sigma_s = \delta\sigma_a + \delta\sigma_G \quad (10)$$

where  $\delta\sigma_a$  and  $\delta\sigma_G$  are the contributions of lattice distortion and modulus distortion to solid solution strengthening.

$$\delta\sigma_a = AG\delta_{ai}^{4/3}c_{ai}^{2/3} \quad (11)$$

$$\delta\sigma_G = AG\delta_{Gi}^{4/3}c_{Gi}^{2/3} \quad (12)$$

where  $A$  is a dimensionless constant,  $G$  is the shear modulus of the alloy,  $c$  is the solute concentration,  $\delta_{ai}$  and  $\delta_{Gi}$  are average atomic size mismatch and average atomic modulus mismatch, respectively [64].  $\delta_{ai}$  and  $\delta_{Gi}$  can be defined via Equations (13) and (14) [63,64].

$$\delta_{ai} = \frac{9}{8} \sum c_j \delta_{a_{ij}} \quad (13)$$

$$\delta_{Gi} = \frac{9}{8} \sum c_j \delta_{G_{ij}} \quad (14)$$

where  $c_j$  is the atomic fraction of  $j$ th element in the alloy,  $r_i$  and  $r_j$  are the atomic radius of  $i$ th and  $j$ th elements, and  $G_i$  and  $G_j$  are the shear modulus of  $i$ th and  $j$ th elements, respectively, and  $\delta_{a_{ij}} = 2(r_i - r_j)/(r_i + r_j)$ ,  $\delta_{G_{ij}} = 2(G_i - G_j)/(G_i + G_j)$ . To facilitate the assessment of the contribution of distortion to HEAs as well as later studies, the value of  $c$  is specified as 0.25.

For ease of calculation, the component ratio is selected as an equivalent component  $Zr_{25}Mo_{25}Ta_{25}W_{25}$ . The calculated atom size distortion and atomic modulus distortion are shown in Table 8. Table 9 shows lattice distortion and modulus distortion near each element in  $Zr_{25}Mo_{25}Ta_{25}W_{25}$  solid solution alloy. The data in Table 8 show that the combined atomic size difference between Mo and W is small, as  $\delta_{a_{ij}} \approx 0.01$ . Compared to the combination with the Zr element, the difference in atomic size between W and Mo is smaller. The size difference between Zr and other elements is as small as  $\delta_{a_{ij}} \approx 0.08$  and up to  $\delta_{a_{ij}} \approx 0.13$ . The lattice distortion near the elements shown in Table 9 is consistent with the above data. The lattice distortion near the Zr element is the greatest,  $\delta_{a_{ij}} \approx 0.096$ . As is expected, the elements with a small radius such as Mo and W produce almost the same local tensile strain,  $|\delta_{a_i}| \sim 0.05$ , while the element with large radius Zr and Ta, produce local compression,  $\delta_{a_i} \sim 0.08\text{--}0.096$ . This local strain is consistent with the lattice distortion near elements in TaNbHfZrTi alloys studied by Senkov et al. [16].

**Table 8.** Atomic size difference  $\delta_{a_{ij}}$  and modulus difference  $\delta_{G_{ij}}$  with bold numbers, of the alloying.

$\delta_{G_{ij}} / \delta_{a_{ij}}$	Zr	Mo	Ta	W
Zr	0	−0.13	−0.08	−0.13
Mo	<b>1.13</b>	0	0.06	0.01
Ta	<b>0.71</b>	<b>−0.52</b>	0	−0.05
W	<b>1.17</b>	<b>0.07</b>	<b>0.59</b>	0

**Table 9.** Calculated lattice distortion  $\delta_{G_i}$  and modulus distortion  $\delta_{G_i}$  near each element in the BCC lattice of the ZrMoTaW alloy.

$\delta_{G_i} / \delta_{a_i}$	Zr	Mo	Ta	W
$\delta_{a_i}$	0.096	−0.056	0.008	−0.047
$\delta_{G_i}$	−0.844	0.446	0.113	0.512

In Table 8, the values of modulus difference between elements range widely, from  $\delta_{G_i} = 0.07$  for the Mo–W atom pair to 1.79 for the Zr–W atom pair. The strongest shear modulus effect of Zr atoms with other elements is that  $\delta_{G_{ij}}$  values range from 0.71 for Zr–Ta to 1.17 for Zr–W, while Mo–W, Mo–Ta, and Ta–W pairs resulted in smaller  $\delta_{G_{ij}}$  values of 0.07, 0.52, and 0.59, respectively. The modulus distortion near the specific element calculated in Table 9 shows that the highest value  $\delta_{G_{Zr}} = 0.844$  is displayed near the Zr atom. Essentially, the Zr interaction produces greater deviations in local forces than the other three elements, resulting in a large effective modulus mismatch. Senkov et al.’s study of Ta has a similar contribution to Zr in this work and they hypothesized that the contribution is mainly derived from Ta. This work assumes that the mismatched contributions are mainly due to Zr. The dimensionless constants A in Equations (11) and (12) take 0.04 [64], and experimentally obtained Er of ZrMoTaW is ~150 GPa, thus the shear modulus G is 56.82 GPa (calculated by  $G = E_r / [2(1 + \nu)]$ ), taking  $\nu$  as 0.32 here). The equiatomic of ZrMoTaW  $c_i$  is 0.25. The resulting atomic size difference contribution is 38.55 MPa and the contribution of the shear modulus is 719.71 MPa. Thus, the dominant contribution to the strengthening is the modulus distortion. The reinforcement effect of this experiment is the same as that of the reported TaNbHfZrTi alloy system [16].

Hardness and modulus have an important influence on wear behavior [65,66]. As mentioned above, the ZrMoTaW film prepared in this work has extremely high hardness, which indicates that the film may have excellent wear resistance. Studies have shown that the ratio of hardness to elastic modulus ( $H/Er$ ) indicates the ability of the material to resist elastic strain before failure [67], and  $H^3/Er^2$  is a plastic deformation factor, which indicates the ability to resist plastic flow [68]. The  $H/Er$  and  $H^3/Er^2$  values are shown in Figure 11, and the higher the ratio of these two values, the better the wear resistance [69]. It can be seen that the ratio of D11 is significantly higher than that of other sample libraries, which means that the wear resistance of D11 is better than that of other areas. This means that ingredients with greater stiffness, modulus, and abrasion resistance can be explored near the area. The highest values of  $H/Er$  and  $H^3/Er^2$  of ZrMoTaW RMPA reached 0.066 and 0.086, respectively, which are significantly higher than ordinary alloys such as ZrCrAlN [70], AlCrSiN [71]. For traditional aluminum-based alloy films, the maximum value of  $H^3/Er^2$  is still lower than 0.02GPa. As a result, the ZrMoTaW RMPEA exhibits excellent protection potential compared to many conventional films. Moreover, the high throughput proposed in this study can quickly identify the property-changing trend brought about by the influence of different elements. It exhibits better hardness and abrasion resistance on the side with high W content.

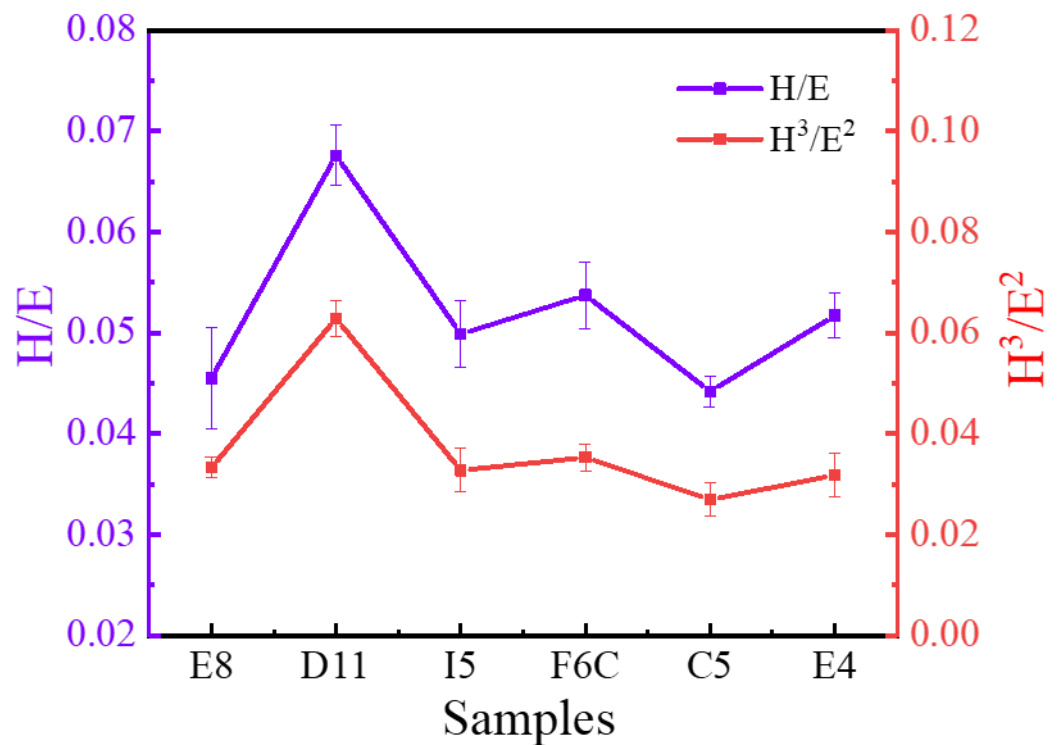


**Figure 11.** Elastic strain to failure,  $H/E$ , and resistance to plastic deformation,  $H^3/E^2$ , of ZrMoTaW RMPEA thin films.

In this work, a thin film library of ZrMoTaW systems with multi-directional gradient components was prepared by multi-gradient deposition combination and porous masking. The results show that:

- (1) By adjusting the power and controlling the distance between the sample and the target, changes in the spatial gradient and composition range can be controlled. The composition of each element changed uniformly in a gradient from different directions. Local uniformity in the element distribution can be observed with the help of SEM surface scanning. This facilitates screening ingredients by demand and exploring the effects of elemental variations.
- (2) The XRD atlas shows that the ZrMoTaW alloy film is a single-phase solid solution with a BCC structure. According to the Hume-Rothery rule, the theoretical parameters of ZrMoTaW alloy thin films  $\Omega \geq 1.1$ ,  $\delta \leq 6.6\%$ ,  $VEC \leq 6.87$ , which meet the conditions for the formation of the BCC solid-solution phase structure. And ZrMoTaW RMPEAs have a high mixing entropy.
- (3) The ZrMoTaW thin films have a nanocrystalline structure with grain sizes of 10–20 nm. The surface morphology of the film shows a flake structure, and the cross-section shows a cylindrical structure. The diffusion of phase separation in HEA is slow. Higher sputtering and deposition rates also refine grains. Multiple factors work synergistically to promote grain refinement.
- (4) The ZrMoTaW thin films have excellent mechanical properties. The component with the highest hardness performance in this film is  $Zr_{11}Mo_{11}Ta_{25}W_{53}$ . The maximum hardness measured is up to 20 GPa, and the modulus of elasticity exceeds 300 GPa. Through quantitative calculations, the main contribution of the film reinforcement produced in this experiment comes from modulus distortion, and it has excellent wear resistance. The  $H/Er$  and  $H^3/Er^2$  of ZrMoTaW RMPEA reached 0.066 and 0.086, respectively.

The structure of ZrMoTaW films will be studied further. The study will be based on the properties of bulk alloys with high W content. Ingredients that are expected to have excellent properties in the film can also be found in the block.

**Author Contributions:** Formal analysis, Q.W.; Investigation, H.Y. and X.Z.; Resources, J.Y.; Data curation, Q.W.; Writing—original draft, Q.W.; Writing—review & editing, Q.W. and Y.W.; Supervision, X.Z. and J.Y.; Funding acquisition, Y.W. All authors have read and agreed to the published version of the manuscript.

**Funding:** The authors gratefully acknowledge to the financial support for this research from Scientific Research Funding Project of the Education Department of Liaoning Province (Grant numbers: LJKZ0123).

**Institutional Review Board Statement:** Not applicable.

**Informed Consent Statement:** Not applicable.

**Acknowledgments:** The authors gratefully acknowledge the financial support for this research from the Scientific Research Funding Project of the Education Department of Liaoning Province (Grant numbers: LJKZ0123).

**Conflicts of Interest:** We declare that we have no financial and personal relationships with other people or organizations that can inappropriately influence our work. There is no professional or other personal interest of any nature or kind in any product, service, and/or company that could be construed as influencing the position presented in, or the review of, the manuscript entitled, “High-throughput preparation method of multi-gradient films and characterization of ZrMoTaW refractory multi-principal element alloy films”.

## References

1. Yeh, J.W.; Chen, S.K.; Lin, S.J.; Gan, J.Y.; Chin, T.S.; Shun, T.T.; Tsau, C.H.; Chang, S.Y. Nanostructured High-Entropy Alloys with Multiple Principal Elements: Novel Alloy Design Concepts and Outcomes. *Adv. Eng. Mater.* **2004**, *6*, 299–303. [[CrossRef](#)]
2. Miracle, D.B.; Senkov, O.N. A critical review of high entropy alloys and related concepts. *Acta Mater.* **2017**, *122*, 448–511. [[CrossRef](#)]
3. Miracle, D.B. Critical Assessment 14: High entropy alloys and their development as structural materials. *Mater. Sci. Technol.* **2015**, *31*, 1142–1147. [[CrossRef](#)]
4. Miracle, D.; Miller, J.; Senkov, O.; Woodward, C.; Uchic, M.; Tiley, J. Exploration and Development of High Entropy Alloys for Structural Applications. *Entropy* **2013**, *16*, 494–525. [[CrossRef](#)]
5. Gorr, B.; Azim, M.; Christ, H.J.; Mueller, T.; Schliephake, D.; Heilmaier, M. Phase equilibria, microstructure, and high temperature oxidation resistance of novel refractory high-entropy alloys. *J. Alloys Compd.* **2015**, *624*, 270–278. [[CrossRef](#)]
6. Mu, Y.; Liu, H.; Liu, Y.; Zhang, X.; Jiang, Y.; Dong, T. An ab initio and experimental studies of the structure, mechanical parameters and state density on the refractory high-entropy alloy systems. *J. Alloys Compd.* **2017**, *714*, 668–680. [[CrossRef](#)]
7. Senkov, O.N.; Scott, J.M.; Senkova, S.V.; Meisenkothen, F.; Miracle, D.B.; Woodward, C.F. Microstructure and elevated temperature properties of a refractory TaNbHfZrTi alloy. *J. Mater. Sci.* **2012**, *47*, 4062–4074. [[CrossRef](#)]
8. Senkov, O.N.; Semiatin, S.L. Microstructure and Properties of a Refractory High-Entropy Alloy after Cold Working. *J. Alloys Compd.* **2015**, *649*, 1110–1123. [[CrossRef](#)]
9. Senkov, O.N.; Senkova, S.V.; Woodward, C. Effect of aluminum on the microstructure and properties of two refractory high-entropy alloys. *Acta Mater.* **2014**, *68*, 214–228. [[CrossRef](#)]
10. Senkov, O.N.; Wilks, G.B.; Miracle, D.B.; Chuang, C.P.; Liaw, P.K. Refractory high-entropy alloys. *Intermetallics* **2010**, *18*, 1758–1765. [[CrossRef](#)]
11. Senkov, O.N.; Wilks, G.B.; Scott, J.M.; Miracle, D.B. Mechanical properties of Nb<sub>25</sub>Mo<sub>25</sub>Ta<sub>25</sub>W<sub>25</sub> and V<sub>20</sub>Nb<sub>20</sub>Mo<sub>20</sub>Ta<sub>20</sub>W<sub>20</sub> refractory high entropy alloys. *Intermetallics* **2011**, *19*, 698–706. [[CrossRef](#)]
12. Tsai, M.H.; Yeh, J.W. High-Entropy Alloys: A Critical Review. *Mater. Res. Lett.* **2014**, *2*, 107–123. [[CrossRef](#)]
13. Yang, X.; Zhang, Y.; Liaw, P.K. Microstructure and Compressive Properties of NbTiVTaAl<sub>x</sub> High Entropy Alloys. *Procedia Eng.* **2012**, *36*, 292–298. [[CrossRef](#)]
14. Zou, Y.; Okle, P.; Yu, H.; Sumigawa, T.; Kitamura, T.; Maiti, S.; Steurer, W.; Spolenak, R. Fracture properties of a refractory high-entropy alloy: In situ micro-cantilever and atom probe tomography studies. *Scr. Mater.* **2017**, *128*, 95–99. [[CrossRef](#)]
15. Wu, S.J.; Wang, X.D.; Lu, J.T.; Qu, R.T.; Zhang, Z.F. Room-Temperature Mechanical Properties of V<sub>20</sub>Nb<sub>20</sub>Mo<sub>20</sub>Ta<sub>20</sub>W<sub>20</sub> High-Entropy Alloy. *Adv. Eng. Mater.* **2018**, *20*, 1800028. [[CrossRef](#)]
16. Senkov, O.N.; Scott, J.M.; Senkova, S.V.; Miracle, D.B.; Woodward, C.F. Microstructure and room temperature properties of a high-entropy TaNbHfZrTi alloy. *J. Alloys Compd.* **2011**, *509*, 6043–6048. [[CrossRef](#)]

17. Wu, Y.D.; Cai, Y.H.; Wang, T.; Si, J.J.; Zhu, J.; Wang, Y.D.; Hui, X.D. A Refractory Hf<sub>25</sub>Nb<sub>25</sub>Ti<sub>25</sub>Zr<sub>25</sub> High-Entropy Alloy with Excellent Structural Stability and Tensile Properties. *Mater. Lett.* **2014**, *130*, 277–280. [[CrossRef](#)]
18. Li, J.; Yang, X.; Zhu, R.; Zhang, Y. Corrosion and Serration Behaviors of TiZr<sub>0.5</sub>NbCr<sub>0.5</sub>V<sub>x</sub>Mo<sub>y</sub> High Entropy Alloys in Aqueous Environments. *Metals* **2014**, *4*, 597–608. [[CrossRef](#)]
19. Chen, T.K.; Shun, T.T.; Yeh, J.W.; Wong, M.S. Nanostructured nitride films of multi-element high-entropy alloys by reactive DC sputtering. *Surf. Coat. Technol.* **2005**, *188*, 193–200. [[CrossRef](#)]
20. Huang, Y.S.; Chen, H.; Lui, H.W.; Yeh, J.W. Microstructure, hardness, resistivity and thermal stability of sputtered oxide films of AlCoCrCu<sub>0.5</sub>NiFe high-entropy alloy. *Mater. Sci. Eng. A* **2007**, *457*, 77–883. [[CrossRef](#)]
21. Yao, C.Z.; Peng, Z.; Meng, L.; Li, G.R.; Ye, J.Q. Electrochemical preparation and magnetic study of Bi–Fe–Co–Ni–Mn high entropy alloy. *Electrochim. Acta* **2008**, *53*, 8359–8365. [[CrossRef](#)]
22. Braic, M.; Braic, V.; Balaceanu, M.; Zoita, C.N.; Grigore, E. Characteristics of (TiAlCrNbY)C films deposited by reactive magnetron sputtering. *Surf. Coat. Technol.* **2010**, *204*, 2010–2014. [[CrossRef](#)]
23. Zhang, Y.; Yan, X.; Ma, J.; Lu, Z.; Zhao, Y. Compositional gradient films constructed by sputtering in a multicomponent Ti–Al–(Cr, Fe, Ni) system. *J. Mater. Res.* **2018**, *33*, 3330–3338. [[CrossRef](#)]
24. Li, M.X.; Sun, Y.T.; Wang, C.; Hu, L.W.; Sohn, S.; Schroers, J.; Wang, W.H.; Liu, Y.H. Data-driven discovery of a universal indicator for metallic glass forming ability. *Nat. Mater.* **2022**, *21*, 165–172. [[CrossRef](#)]
25. Feng, X.; Tang, G.; Gu, L.; Ma, X.; Sun, M.; Wang, L. Preparation and characterization of TaNbTiW multi-element alloy films. *Appl. Surf. Sci.* **2012**, *261*, 447–453. [[CrossRef](#)]
26. Khan, N.A.; Akhavan, B.; Zhou, H.; Chang, L.; Wang, Y.; Sun, L.; Bilek, M.M.; Liu, Z. High entropy alloy thin films of AlCoCrCu<sub>0.5</sub>FeNi with controlled microstructure. *Appl. Surf. Sci.* **2019**, *495*, 143560. [[CrossRef](#)]
27. Sha, C.; Zhou, Z.; Xie, Z.; Munroe, P. FeMnNiCoCr-based high entropy alloy coatings: Effect of nitrogen additions on microstructural development, mechanical properties and tribological performance. *Appl. Surf. Sci.* **2020**, *507*, 145101. [[CrossRef](#)]
28. Paulius, M.; Stefan, F.; Lars, R.; Linus, V.; Johan, C.; David, R.; Leif, N.; Erik, L. Synthesis and characterization of multicomponent (CrNbTaTiW)C films for increased hardness and corrosion resistance. *Mater. Des.* **2018**, *149*, 51–62.
29. Nagender-Naidu, S.V.; Sriramamurthy, A.M.; Rao, P.R. The Mo–W (Molybdenum–Tungsten) System. *J. Phase Equilibria Diffus.* **1984**, *5*, 177–180. [[CrossRef](#)]
30. Schramm, C.H.; Gordon, P.; Kaufmann, A. The alloy systems uranium-tungsten, uranium-tantalum and tungsten-tantalum. *J. Met.* **1950**, *2*, 195–204. [[CrossRef](#)]
31. Rajkumar, V.B.; Du, Y.; Liu, S.; Cheng, K.; Srivastav, A.K. Measurements of the melting points, liquidus, and solidus of the Mo, Ta, and Mo–Ta binary alloys using a novel high-speed pyrometric technique. *Int. J. Refract. Met. H.* **2020**, *93*, 105335. [[CrossRef](#)]
32. Pease, L.F.; Brophy, J.H. The zirconium-tungsten-tantalum system. *J. Less Common Metals* **1964**, *6*, 118–131. [[CrossRef](#)]
33. Deboer, F.R. *Cohesion in Metals*; Elsevier Scientific Pub. Co.: New York, NY, USA, 1989; Volume 544.
34. Porter, D.A.; Easterling, K.E. *Phase Transformations in Metals and Alloys*; CRC Press: Boca Raton, FL, USA, 2019.
35. Sheng, G.; Ng, C.; Jian, L.; Liu, C.T. Effect of valence electron concentration on stability of fcc or bcc phase in high entropy alloys. *J. Appl. Phys.* **2011**, *109*, 213.
36. Maiti, S.; Steurer, W. Structural-disorder and its effect on mechanical properties in single-phase TaNbHfZr high-entropy alloy. *Acta Mater.* **2016**, *106*, 87–97. [[CrossRef](#)]
37. Yong, Z.; Yun, J.Z. Solid Solution Formation Criteria for High Entropy Alloys. *Mater. Sci. Forum.* **2007**, *561–565*, 1337–1339.
38. Yong, Z.; Yun, J.Z.; Lin, J.P.; Chen, G.L.; Liaw, P.K. Solid-Solution Phase Formation Rules for Multi-component Alloys. *Adv. Eng. Mater.* **2008**, *10*, 534–538.
39. Kittel, C. *Introduction to Solid State Physics*; Wiley: New York, NY, USA, 1996; p. 21.
40. Yang, X.; Zhang, Y. Physics, Prediction of high-entropy stabilized solid-solution in multi-component alloys. *Mater. Chem. Phys.* **2012**, *132*, 233–238. [[CrossRef](#)]
41. Ye, G.; Lee, D.N. Orientation and microstructure of dull nickel electrodeposits. *Plat. Surf. Finish.* **1981**, *68*, 60–64.
42. Sheng, W.; Yang, X.; Wang, C.; Zhang, Y. Nano-Crystallization of High-Entropy Amorphous NbTiAlSiW<sub>x</sub>N<sub>y</sub> Films Prepared by Magnetron Sputtering. *Entropy* **2016**, *18*, 226. [[CrossRef](#)]
43. Peng, X.; Chen, L. Effect of high entropy alloys TiVCrZrHf barrier layer on microstructure and texture of Cu thin films. *Mater. Lett.* **2018**, *230*, 5–8. [[CrossRef](#)]
44. Chandra, R.; Chawla, A.K.; Kaur, D.; Ayyub, P. Structural, optical and electronic properties of nanocrystalline TiN films. *Nanotechnology* **2005**, *16*, 3053. [[CrossRef](#)]
45. Zhang, Y.; Xu, Z.; Zhang, Z.; Yao, W.; Hui, X.; Liang, X. Microstructure and mechanical properties of Mo–Ta–W refractory multi-principal element alloy thin films for hard protective coatings. *Surf. Coat. Technol.* **2022**, *431*, 128005. [[CrossRef](#)]
46. Song, B.; Li, Y.; Cong, Z.; Li, Y.; Song, Z.; Chen, J. Effects of deposition temperature on the nanomechanical properties of refractory high entropy TaNbHfZr films. *J. Alloys Compd.* **2019**, *797*, 1025–1030. [[CrossRef](#)]
47. Zhang, J.Y.; Cui, J.C.; Liu, G.; Sun, J. Deformation crossover in nanocrystalline Zr micropillars: The strongest external size. *Scripta Mater.* **2013**, *68*, 639–642. [[CrossRef](#)]
48. Kaufmann, D.; Schneider, A.S.; Mönig, R.; Volkert, C.A.; Kraft, O. Effect of surface orientation on the plasticity of small bcc metals. *Int. J. Plast.* **2013**, *49*, 145–151. [[CrossRef](#)]

49. Kim, J.; Jang, D.; Greer, J. Tensile and compressive behavior of tungsten, molybdenum, tantalum and niobium at the nanoscale. *Acta Mater.* **2010**, *58*, 2355–2363. [[CrossRef](#)]
50. Schneider, A.S.; Clark, B.G.; Frick, C.P.; Gruber, P.A.; Arzt, E. Correlation between Critical Temperature and Strength of Small-Scale bcc Pillars. *Phys. Rev. Lett.* **2009**, *103*, 105501. [[CrossRef](#)]
51. Feng, X.B.; Zhang, J.Y.; Wang, Y.Q.; Hou, Z.Q.; Wu, K.; Liu, G.; Sun, J. Size effects on the mechanical properties of nanocrystalline NbMoTaW refractory high entropy alloy thin films. *Int. J. Plast.* **2017**, *95*, 264–277. [[CrossRef](#)]
52. Chang, Z.C.; Liang, S.C.; Han, S.; Chen, Y.K.; Shieu, F.S. Characteristics of TiVCrAlZr multi-element nitride films prepared by reactive sputtering. *Nucl. Instrum. Methods Phys. Res. Sect. B* **2010**, *268*, 2504–2509. [[CrossRef](#)]
53. Zou, Y.; Ma, H.; Spolenak, R. Ultrastrong ductile and stable high-entropy alloys at small scales. *Nat. Protoc.* **2015**, *6*, 7748. [[CrossRef](#)]
54. Liao, W.; Lan, S.; Gao, L.; Zhang, H.; Xu, S.; Song, J.; Wang, X.; Lu, Y. Nanocrystalline high-entropy alloy (CoCrFeNiAl<sub>0.3</sub>) thin-film coating by magnetron sputtering. *Thin Solid Films* **2017**, *638*, 383–388. [[CrossRef](#)]
55. Li, W.; Liu, P.; Liaw, P.K. Microstructures and properties of high-entropy alloy films and coatings: A review. *Mater. Res. Lett.* **2018**, *6*, 199–229. [[CrossRef](#)]
56. Lai, C.H.; Lin, S.J.; Yeh, J.W. Effect of substrate bias on the structure and properties of multi-element (AlCrTaTiZr)N coatings. *J. Phys. D Appl. Phys.* **2006**, *39*, 4628–4633. [[CrossRef](#)]
57. Jiang, W.G.; Su, J.J.; Feng, X.Q. Effect of surface roughness on nanoindentation test of thin films. *Eng. Fract. Mech.* **2008**, *75*, 4965–4972. [[CrossRef](#)]
58. Liu, L.; Zhu, J.B.; Hou, C.; Li, J.C.; Jiang, Q. Dense and smooth amorphous films of multicomponent FeCoNiCuVZrAl high-entropy alloy deposited by direct current magnetron sputtering. *Mater. Des.* **2013**, *46*, 675–679. [[CrossRef](#)]
59. Sheng, W.J.; Yang, X.; Zhu, J.; Wang, C.; Zhang, Y. Amorphous phase stability of NbTiAlSiNX high-entropy films. *Rare Metals* **2018**, *37*, 682–689. [[CrossRef](#)]
60. Guo, W.; Dmowski, W.; Noh, J.Y.; Rack, P.; Liaw, P.K.; Egami, T. Local Atomic Structure of a High-Entropy Alloy: An X-Ray and Neutron Scattering Study. *Metall. Mater. Trans. A* **2013**, *44*, 1994–1997. [[CrossRef](#)]
61. Yeh, J.W.; Chang, S.Y.; Hong, Y.D.; Chen, S.K.; Lin, S.J. Anomalous decrease in X-ray diffraction intensities of Cu–Ni–Al–Co–Cr–Fe–Si alloy systems with multi-principal elements. *Mater. Chem. Phys.* **2007**, *103*, 41–46. [[CrossRef](#)]
62. Isaac, T.C.; Rivera-Díaz-del-Castillo, P.E. Modelling solid solution hardening in high entropy alloys. *Acta Mater.* **2015**, *85*, 14–23.
63. Lee, C.; Song, G.; Gao, M.C.; Feng, R.; Chen, P.; Brechtel, J.; Chen, Y.; An, K.; Guo, W.; Poplawsky, J.D.; et al. Lattice distortion in a strong and ductile refractory high-entropy alloy. *Acta Mater.* **2018**, *160*, 158–172. [[CrossRef](#)]
64. Yao, H.W.; Qiao, J.W.; Hawk, J.A.; Zhou, H.F.; Chen, M.W.; Gao, M.C. Mechanical properties of refractory high-entropy alloys: Experiments and modeling. *J. Alloys Compd.* **2017**, *696*, 1139–1150. [[CrossRef](#)]
65. Chen, C.Q.; Pei, Y.T.; Shaha, K.P.; De Hosson, J.T.M. Nanoscale deformation mechanism of TiC/a-C nanocomposite thin films. *J. Appl. Phys.* **2009**, *105*, 114314. [[CrossRef](#)]
66. Galvan, D.; Pei, Y.T.; De Hosson, J.T.M. Deformation and failure mechanism of nano-composite coatings under nano-indentation. *Surf. Coat. Technol.* **2006**, *200*, 6718–6726. [[CrossRef](#)]
67. Leyland, A.; Matthews, A. On the significance of the H/E ratio in wear control: A nanocomposite coating approach to optimised tribological behaviour. *Wear* **2000**, *246*, 1–11. [[CrossRef](#)]
68. Mayrhofer, P.H.; Mitterer, C.; Musil, J. Structure–property relationships in single- and dual-phase nanocrystalline hard coatings. *Surf. Coat. Technol.* **2003**, *174–175*, 725–731. [[CrossRef](#)]
69. Li, W.Z.; Liu, H.W.; Evaristo, M.; Polcar, T.; Cavaleiro, A. Chemical state, structure and mechanical properties of multi-element (CrTaNbMoV)N<sub>x</sub> films by reactive magnetron sputtering. *Mater. Chem. Phys.* **2020**, *239*, 121991.
70. Briois, P.; Mercks, D.; Banakh, O.; Lamy, S.; Steinmann, P.A.; Coddet, C. Influence of Al content on the mechanical properties and thermal stability in protective and oxidation atmospheres of Zr–Cr–Al–N coatings. *Surf. Coat. Technol.* **2013**, *236*, 239–245.
71. Feng, X.B.; Zhang, J.Y.; Wang, Y.Q.; Hou, Z.Q.; Wu, K.; Liu, G.; Sun, J. Structural and Mechanical Properties of (Al,Cr)N and (Al,Cr)SiN Coatings Reactively Sputter Deposited. *Plasma Process Polym.* **2007**, *4* (Suppl. S1), S677–S680.